Efficient Simulation of Multi-Body Contact Problems on Complex Geometries: A Flexible Decomposition Approach Using Constrained Minimization

Thomas Dickopf, Rolf Krause

no. 388

Diese Arbeit ist mit Unterstützung des von der Deutschen Forschungsgemeinschaft getragenen Sonderforschungsbereichs 611 an der Universität Bonn entstanden und als Manuskript vervielfältigt worden.

Bonn, März 2008

EFFICIENT SIMULATION OF MULTI-BODY CONTACT PROBLEMS ON COMPLEX GEOMETRIES: A FLEXIBLE DECOMPOSITION APPROACH USING CONSTRAINED MINIMIZATION*

THOMAS DICKOPF AND ROLF KRAUSE†

Abstract. We consider the numerical simulation of nonlinear multi-body contact problems in elasticity on complex three-dimensional geometries. In the case of warped contact boundaries and non-matching finite element meshes, particular emphasis has to be put on the discretization of the transmission of forces and the non-penetration conditions at the contact interface. We enforce the discrete contact constraints by means of a non-conforming domain decomposition method, which allows for optimal error estimates. Here, we develop an efficient method to assemble the discrete coupling operator by computing the triangulated intersection of opposite element faces in a locally adjusted projection plane but carrying out the required quadrature on the faces directly. Our new element-based algorithm does not use any boundary parametrizations and is also suitable for isoparametric elements. The emerging nonlinear system is solved by a monotone multigrid method of optimal complexity. Several numerical examples in 3D illustrate the effectiveness of our approach.

Key words. contact problems, linear elasticity, finite elements, non-matching meshes, domain decomposition, mortar methods, multigrid methods

AMS subject classifications. 65N30, 65N55, 74B05, 74S05

1. Introduction.

The numerical simulation of contact problems in elasticity certainly is a topic of current research. In case the impact of two or more deformable bodies on each other shall be examined, the discrete information transfer across the contact interfaces turns out to be crucial for both, the quality and the efficiency of a numerical approximation. Previous approaches predominantly deal with a highly simplified setting of a priori matching contact boundaries, see, e. g., [5, 12, 22, 24, 38]. Thus, they fail or cannot be used in case of the complex geometries occuring in realistic, three-dimensional simulations and new methods have to be developed. In particular, we have to give attention to warped contact boundaries with non-matching finite element meshes and, actually, geometrically non-matching interfaces.

In spite of the usual linearizations in the strain tensor and the constitutive law, the free boundary problem arising from the additional contact constraints is nonlinear. We approximate the geometrical non-penetration condition by pointwise inequality constraints, using a bijective contact mapping $\mathbf{\Phi}$. Therefore, the multi-body contact problem can be written as a variational inequality on the convex set of admissible displacements and the existence of a unique solution results from an application of well-established instruments from convex analysis, see, e. g., [9, 14, 39].

In this paper, the discretization of the coupling constraints is done in a weak sense by a modified mortar finite element method, see, e. g., [4, 5, 7], proposing the use of an L^2-projection between non-matching meshes to allow for optimal error estimates. Here, motivated by [15, 33, 41, 42], we develop an efficient method to compute the emerging discrete transfer operator for complex geometries. We compute triangulated intersections of opposite element faces in a locally adjusted projection plane but carry out the necessary numerical quadrature on possibly warped contact boundaries directly.

*This work was supported in part by the Deutsche Forschungsgemeinschaft via SFB 611, Hausdorff Center for Mathematics, and Bonn International Graduate School in Mathematics.

†University of Bonn, Institute for Numerical Simulation, Wegelerstraße 6, 53115 Bonn, Germany (dickopf@ins.uni-bonn.de, krause@ins.uni-bonn.de)

Going beyond [41], we give a sound derivation of our element-based algorithm, which computes the discrete coupling between two arbitrary interfaces from local information exclusively. The analysis we carry out provides an interpretation of the method as a construction of a global a priori approximation of the real contact mapping $\boldsymbol{\Phi}$ by a composition of local projections and inverse projections. That closes the gap to [33]. We note that no parametrizations of any kind are needed. Besides, our method is also applicable to isoparametric finite elements.

By now, various methods for the iterative solution of the discretized contact problem have been developed, such as penalty methods, augmented Lagrangian approaches, active set strategies, and nonlinear Dirichlet-Neumann algorithms, see, e. g., [15, 27, 34, 36, 37, 46]. Here, we employ a local basis transformation from [45] using the discrete transfer operator and solve the emerging system by an adaptive monotone multigrid method of optimal complexity, see [30, 31]. The method does neither use regularization nor an outer iteration but, instead, deals with the constraints locally by means of a nonlinear block Gauß-Seidel smoother on the finest grid.

Note that the coupling approach is in no way limited to contact mechanics. Whenever discrete quantities, vectorial or scalar, have to be transferred between finite element meshes on geometrically non-matching interfaces, one should regard our L^2-projection as a possibility to realize that in an efficient way. An extension to the information transfer between non-nested volume meshes is also practicable.

The rest of this paper is organized as follows. In Section 2, we state the multi-body contact problem as a variational inequality over the convex set of admissible displacements incorporating the contact constraints. In Section 3, a non-conforming approximation by a mortar finite element approach is specified, where the discrete contact conditions are efficiently realized by a weak coupling. In Section 4, we develop a method for the computation of the discrete transfer operator. A sound derivation as well as a detailed analysis of the algorithm are given. Section 5 is devoted to the iterative solution of the emerging nonlinear system by constrained multilevel energy minimization. Finally, in Section 6, we present several numerical results illustrating the effectivity of our approach.

2. Problem formulation. In this section, we give the strong and the weak formulation of the multi-body contact problem in linear elasticity. Equilibrium, boundary, and contact conditions are addressed and the groundwork for the disretization in the next section is done. Special attention is paid to a more general formulation of the linearized non-penetration condition.

We consider the deformation of two bodies, which in their reference configuration are identified with the Lipschitz domains $\Omega^m, \Omega^s \subset \mathbb{R}^3$, where the indices m and s are motivated by the master and slave role the subdomains will play in the subsequent sections. The restriction to two-body contact is imposed for the ease of presentation only. The displacement field $\boldsymbol{u}$, decomposed into $\boldsymbol{u} = (\boldsymbol{u}^m, \boldsymbol{u}^s)$, is given as the solution of the boundary value problem

$$\begin{aligned} -\sigma_{ij}(\boldsymbol{u})_{,j} &= f_i \quad \text{in } \Omega, \\ \boldsymbol{u} &= \boldsymbol{0} \quad \text{on } \Gamma_D, \\ \sigma_{ij}(\boldsymbol{u})n_j &= p_i \quad \text{on } \Gamma_N. \end{aligned} \tag{1}$$

Here, the boundary $\Gamma = \Gamma^m \cup \Gamma^s$ of $\Omega = \Omega^m \cup \Omega^s$ consists of three pairwise disjoint parts, $\Gamma_D = \Gamma_D^m \cup \Gamma_D^s$ the Dirichlet boundary, which is assumed to be of positive two-dimensional Lebesgue measure on both bodies, $\Gamma_N = \Gamma_N^m \cup \Gamma_N^s$ the Neumann boundary, and $\Gamma_C = \Gamma_C^m \cup \Gamma_C^s$ the possible contact boundary with $\Gamma_\bullet^k := \Gamma_\bullet \cap \Omega^k$,

$k \in \{m, s\}$, $\bullet \in \{C, D, N\}$. Additionally, the condition $\overline{\Gamma}_C \cap \overline{\Gamma}_D = \emptyset$ may hold, which appears to be quite natural in most applications. The actual contact boundary is not known in advance but at least assumed to be compactly embedded in Γ_C. On the right hand side we have the volume force density $\boldsymbol{f} \in \boldsymbol{L}^2(\Omega)$ and the prescribed surface traction density $\boldsymbol{p} \in \boldsymbol{L}^2(\Gamma_N)$ the bodies are subjected to. The vector $\boldsymbol{n} = (\boldsymbol{n}^m, \boldsymbol{n}^s)$ is the outer normal on Γ.

We denote vector quantities by bold symbols, e. g., $\boldsymbol{v}$, and their i-th component by v_i. Analogously, we use bold symbols for vector valued function spaces, i. e. $\boldsymbol{V} := (V)^3$. The partial derivative with respect to x_j is abbreviated with the index $_{,j}$. Furthermore, we enforce the summation convention on all repeated indices ranging from 1 to 3 and denote by δ_{ij} the Kronecker symbol. The standard basis of $\mathbb{R}^3$ will be referred to as $(\boldsymbol{e}_i)_{1 \le i \le 3}$. We write $\boldsymbol{I}$ for the identity matrix.

The materials are assumed to be linear elastic, homogeneous, and isotropic with strainless reference configuration, so that by Hooke's law the stress tensor $\boldsymbol{\sigma}$ can be written as

$$\sigma_{ij}(\boldsymbol{u}) = A_{ijlm} u_{l,m} = \frac{E\nu}{(1+\nu)(1-2\nu)} \delta_{ij} \epsilon_{kk}(\boldsymbol{u}) + \frac{E}{1+\nu} \epsilon_{ij}(\boldsymbol{u}),$$

where $\boldsymbol{\epsilon}(\boldsymbol{u}) := \frac{1}{2}(\boldsymbol{\nabla u} + \boldsymbol{\nabla u}^T)$ denotes the infinitesimal strain tensor, $E > 0$ is Young's modulus, and $0 < \nu < \frac{1}{2}$ is the Poisson ratio. Hooke's tensor $\boldsymbol{A} := (A_{ijlm})$ is sufficiently smooth, i. e. $A_{ijlm} \in L^\infty(\Omega)$, $1 \le i, j, l, m \le 3$, symmetric, and uniformly positive definite. For introductions to (contact) mechanics we refer to the monographs [11, 28, 36, 46], which consider this subject from the mathematician's as well as the engineer's point of view.

In contrast to many other presentations we neither restrict ourselves to the case where the two possible contact boundaries Γ_C^m and Γ_C^s coincide in the reference configuration nor require (one of) them to be planar. In order to prescribe additional boundary conditions, which reflect the forces evolving because of the contact of the two bodies, we rather assume, similar to [14], a smooth, bijective mapping $\boldsymbol{\Phi} : \Gamma_C^s \to \Gamma_C^m$ to be given, which relates every point on Γ_C^s to a potential contact point on Γ_C^m. Naturally being a part of the solution, such a contact mapping is not achievable a priori. Nevertheless, at this stage we will use it to derive the contact conditions and discuss reasonable discrete versions later on. Now, we can define a vector field of contact directions

$$\boldsymbol{n}^\Phi : \Gamma_C^s \to \mathbb{S}^2, \quad \boldsymbol{n}^\Phi(\boldsymbol{x}) := \begin{cases} \frac{\boldsymbol{\Phi}(\boldsymbol{x}) - \boldsymbol{x}}{|\boldsymbol{\Phi}(\boldsymbol{x}) - \boldsymbol{x}|}, & \text{if } \boldsymbol{\Phi}(\boldsymbol{x}) \neq \boldsymbol{x}, \\ \boldsymbol{n}^s(\boldsymbol{x}), & \text{otherwise,} \end{cases}$$

and the initial gap function $g : \Gamma_C^s \to \mathbb{R}_+$, $g(\boldsymbol{x}) := |\boldsymbol{\Phi}(\boldsymbol{x}) - \boldsymbol{x}|$, which is equal to the distance between Γ_C^s and Γ_C^m according to the contact mapping. Then, the jump of the solution and its component in $\boldsymbol{n}^\Phi$-direction, respectively, are

$$[\boldsymbol{u}] := \boldsymbol{u}^s - \boldsymbol{u}^m \circ \boldsymbol{\Phi}, \quad [u] := [\boldsymbol{u}] \cdot \boldsymbol{n}^\Phi,$$

and the linearized contact conditions on Γ_C can be written as

$$\begin{array}{rcccll} \boldsymbol{\sigma}_t(\boldsymbol{u}^m) & = & \boldsymbol{\sigma}_t(\boldsymbol{u}^s) & = & \boldsymbol{0} & \text{on } \Gamma_C, \\ \sigma_n(\boldsymbol{u}^m \circ \boldsymbol{\Phi}) & = & \sigma_n(\boldsymbol{u}^s) & \le & 0 & \text{on } \Gamma_C^s, \end{array} \tag{2}$$

and

$$[u] \le g, \quad ([u] - g)\sigma_n(\boldsymbol{u}^s) = 0 \quad \text{on } \Gamma_C^s, \tag{3}$$

where $\sigma_n := \sigma_{ij} n_j n_i$ and $((\boldsymbol{\sigma}_t)_i)_{1\le i\le 3} := (\sigma_{ij} n_j - \sigma_n n_i)_{1\le i\le 3}$ are the normal and tangential parts of $\boldsymbol{\sigma}$, respectively. By $(2)_1$ we state contact without friction, whereas $(2)_2$ reflects Newton's third law. Only considering the frictionless case in this paper, we refer to [14] and the above-mentioned monographs for the modeling of frictional phenomena.

The geometric contact condition $\Omega^m \cap \Omega^s = \emptyset$, which is nonlinear and has global character, has been approximated by the pointwise inequality $(3)_1$ enforcing non-penetration with respect to the given contact mapping. If points only move in $\boldsymbol{n}^\Phi$-direction, this linearization reproduces the non-penetration condition exactly. This is in general not the case, but the author of [14] proves under mild requirements on Γ_C and the corresponding normal fields that the two conditions are equivalent for small displacements except for a bounded error. Finally, $(3)_2$ is the usual Kuhn-Tucker condition.

To obtain a variational formulation of the two-body contact problem, we introduce the Sobolev spaces $\boldsymbol{H}^1_D(\Omega^k) := \left\{\boldsymbol{v} \in \boldsymbol{H}^1(\Omega^k) \middle|\, \boldsymbol{v} = \boldsymbol{0},\ \text{a. e. on } \Gamma^k_D\right\}$, $k \in \{m, s\}$, satisfying homogeneous Dirichlet boundary conditions on Γ_D. Then, incorporating the non-penetration condition, we get the closed and convex set of admissible displacements

$$\mathcal{K} := \{\boldsymbol{v} \in \boldsymbol{X} \,|\, [v] \le g,\ \text{a. e. on } \Gamma^s_C\}$$

with $\boldsymbol{X} := \prod_{k\in\{m,s\}} \boldsymbol{H}^1_D(\Omega^k)$. By the assumption that the contact mapping $\boldsymbol{\Phi}$ a priori indentifies the points coming into contact with each other, we have transformed the geometric non-penetration condition into a pointwise inequality on Γ^s_C only. Therefore, we can verify the convexity of $\mathcal{K}$ straightforwardly.

We define the bilinear form

$$a : \boldsymbol{X} \times \boldsymbol{X} \to \mathbb{R}, \quad a(\boldsymbol{u}, \boldsymbol{v}) := \sum_{k\in\{m,s\}} \int_{\Omega^k} A_{ijlm} u_{l,m} v_{i,j}\, d\boldsymbol{x}$$

and the linear form

$$f : \boldsymbol{X} \to \mathbb{R}, \quad f(\boldsymbol{v}) := \sum_{k\in\{m,s\}} \left(\int_{\Omega^k} f^k_i v^k_i\, d\boldsymbol{x} + \int_{\Gamma^k_N} p^k_i v^k_i\, d\boldsymbol{a} \right).$$

It can be shown, see, e. g., [9] for details, that the solution of the boundary value problem (1), (2), and (3) can be characterized by the following variational inequality: Find $\boldsymbol{u} \in \mathcal{K}$ so that

$$a(\boldsymbol{u}, \boldsymbol{v} - \boldsymbol{u}) \ge f(\boldsymbol{v} - \boldsymbol{u}), \quad \forall\, \boldsymbol{v} \in \mathcal{K}. \tag{4}$$

The unique solvability of problem (4) follows from Lions' and Stampacchia's lemma, see [39], since for positive measure of Γ^m_D and Γ^s_D the strong convexity of the functional $J(\boldsymbol{u}) := \frac{1}{2} a(\boldsymbol{u}, \boldsymbol{u}) - f(\boldsymbol{u})$ is a consequence of Korn's inequality. Admittedly, this does not include any information about the smoothness of the solution. But in [9] at least local $\boldsymbol{H}^2$-regularity of $\boldsymbol{u}$ is shown.

3. Mortar finite element approximation. By now, the finite element method is a widely spread and intensively studied procedure to gain a numerical approximation of a system of partial differential equations. But only by using more sophisticated methods such as modern domain decomposition techniques, one can achieve a discretization of the multi-body contact problem with optimal error estimates. Here,

the discrete information transfer by means of discretizing the coupling constraints and modeling the transmission of forces between the respective bodies, is of major importance for the quality of the approximation.

The mortar method has originally been introduced by Bernardi, Maday, and Patera [7] as a domain decomposition technique for linear problems handling both, functional and geometrical non-conformity. In the meantime, much work has been done transferring the method to various problem classes. For a recent overview and an illustration of the flexibility of the approach see [8]. In this paper, we only make use of the application to discretizations by finite elements with non-matching meshes, see, e. g., [4, 6, 10, 37].

For a more comprehensive work in this area and the introduction of dual multiplier spaces we refer to Wohlmuth [44], who also addresses higher order discretizations and multigrid methods for mortar formulations. Especially the choice of an appropriate multiplier space is still subject of actual research, see [18, 19, 29, 35]. Furthermore, mortar finite elements have successfully been adopted to variational inequalities originating from contact problems, see, e. g., [5, 12, 26, 45].

The construction of the finite element discretization of the contact problem, we present in this section, is motivated by the following understanding: with non-matching meshes a pointwise coupling of the solution across the interfaces as in [21] yields indeed a conforming approximation but does not provide optimal discretization error estimates, see [23] for a counter-example. So, instead of enforcing continuity of the solution, we impose a weak matching condition by the introduction of suitable Lagrange multipliers on the contact boundary. This approach permits a proof of the optimality of the discretization error, since the best approximation error as well as the additionally caused consistency error are of optimal order.

3.1. Realization of the contact conditions by Lagrange multipliers. Let $\mathcal{T}^k$ be a shape regular mesh of Ω^k, $k \in \{m, s\}$, made up of tetrahedrons, hexahedrons, pyramids, and prisms, so that $\Omega^k = \cup_{T\in\mathcal{T}^k} T$. We denote the nodes of $\mathcal{T}^k$ by $\mathcal{N}^k$ and set $\mathcal{N}^k_\bullet := \mathcal{N}^k \cap \Gamma_\bullet$, $k \in \{m, s\}$, $\bullet \in \{C, D, N\}$. On both subdomains, we use $\boldsymbol{X}_h(\Omega^k) := (X_h(\Omega^k))^3$ the space of Lagrangian conforming finite elements of first order and denote its nodal basis functions as $(\lambda^k_p \boldsymbol{e}_i)_{p\in\mathcal{N}^k, 1\le i\le 3}$ with $\lambda^k_p(q) = \delta_{pq}$, $p, q \in \mathcal{N}^k$, $k \in \{m, s\}$. Then, the unconstrained product finite element space is given as $\boldsymbol{X}_h := \prod_{k\in\{m,s\}} \boldsymbol{X}_h(\Omega^k)$. All finite element functions will be marked by the subscript $_h$.

Now, we derive a discrete variant of the contact conditions (2), (3). A particular advantage of our approach to be presented here is that it incorporates the original intention of the mortar method in the context of domain decomposition as well as the contact case. For this purpose and to allow for a generalization to contact with friction, we follow the traditional mortar ansatz and define a vector valued space $\boldsymbol{M}_h$ of Lagrange multipliers on Γ^s_C, which will be used to impose weak matching conditions. Let $\boldsymbol{X}_h(\Gamma^k_C)$ be the trace space of $\boldsymbol{X}_h(\Omega^k)$ on Γ^k_C, $k \in \{m, s\}$. Then, we choose the trace space on Γ^s_C as multiplier space, i. e. $\boldsymbol{M}_h := \boldsymbol{X}_h(\Gamma^s_C)$, and fix a basis $(\psi_p \boldsymbol{e}_i)_{p\in\mathcal{N}^s_C, 1\le i\le 3}$. Because the multiplier space is associated with the mesh inherited from $\mathcal{T}^s$ and because the displacements on Γ^m_C will constrain the displacements on Γ^s_C, we call entities with superscript ^{s} slave (or non-mortar), whereas entities with superscript ^{m} are referred to as master (or mortar).

The standard approach is $\psi_p := \lambda^s_p$, $p \in \mathcal{N}^s_C$, where we note that unlike the standard mortar method no modification of multipliers near the boundary of Γ^s_C is necessary, since $\overline{\Gamma}_C \cap \overline{\Gamma}_D = \emptyset$. Another popular choice, we consider later on, is a space of dual Lagrange multipliers introduced by Wohlmuth, which meets a biorthogonality

relation to the nodal basis. For a rigorous analysis of these multiplier spaces we refer to [44].

The well-known weak "zero jump condition" of the mortar method from [7], which leads to a non-conforming approximation of the space $\boldsymbol{H}^1_D(\mathrm{int}(\overline{\Omega}^m \cup_\Phi \overline{\Omega}^s))$ with optimal discretization error, is

$$\int_{\Gamma_C^s} \boldsymbol{\psi}_h \cdot [\boldsymbol{u}_h]\, d\boldsymbol{a} = 0, \quad \forall\, \boldsymbol{\psi}_h \in \boldsymbol{M}_h, \tag{5}$$

where $\cup_\Phi$ indicates the union with identification of points on Γ_C by $\boldsymbol{\Phi}$. Inspired by these weak coupling constraints, we use the representations of $\boldsymbol{u}_h$ and $\boldsymbol{\psi}_h$ in the chosen bases of $\boldsymbol{X}_h$ and $\boldsymbol{M}_h$, respectively, and define the discrete mortar transfer operator via its algebraic representation, $\boldsymbol{T} := \boldsymbol{D}^{-1}\boldsymbol{B}$, with 3×3-block entries

$$\boldsymbol{d}_{pq} := \int_{\Gamma_C^s} \psi_p \lambda_q^s \, d\boldsymbol{a}\, \boldsymbol{I}, \quad p, q \in \mathcal{N}_C^s, \tag{6}$$

and

$$\boldsymbol{b}_{pq} := \int_{\Gamma_C^s} \psi_p (\lambda_q^m \circ \boldsymbol{\Phi})\, d\boldsymbol{a}\, \boldsymbol{I}, \quad p \in \mathcal{N}_C^s, q \in \mathcal{N}_C^m. \tag{7}$$

The transfer operator $\boldsymbol{T}$ maps a vector of discrete displacements in the trace space $\boldsymbol{X}_h(\Gamma_C^m)$ on the master side via the multiplier space $\boldsymbol{M}_h$ to the trace space $\boldsymbol{X}_h(\Gamma_C^s)$ on the slave side. More precisely, for $\boldsymbol{v}^m \in \boldsymbol{X}_h(\Gamma_C^m)$ the function $\boldsymbol{T}\boldsymbol{v}^m$ is the $\boldsymbol{L}^2$-projection of $\boldsymbol{v}^m \circ \boldsymbol{\Phi}$ onto $\boldsymbol{X}_h(\Gamma_C^s)$.

To enforce discrete contact conditions comparable to (2) and (3), we do not require a zero jump as in (5). Instead, we consider a scalar space M_h of Lagrange multipliers, which is the positive part of $\boldsymbol{M}_h$ in direction of $\boldsymbol{n}^\Phi$, containing the discrete normal stresses,

$$M_h := \left\{ \psi_h = \boldsymbol{\psi}_h' \cdot \boldsymbol{n}^\Phi \,|\, \boldsymbol{\psi}_h' \in \boldsymbol{M}_h,\ \int_{\Gamma_C^s} \psi_h \lambda_h \, d\boldsymbol{a} \geq 0,\ \forall\, \lambda_h \in X_h(\Gamma_C^s),\ \lambda_h \geq 0 \right\}.$$

Then, the non-penetration condition reads as

$$\int_{\Gamma_C^s} ([u_h] - g)\psi_h \, d\boldsymbol{a} \leq 0, \quad \forall\, \psi_h \in M_h, \tag{8}$$

where only inequality constraints in $\boldsymbol{n}^\Phi$-direction are imposed. We use the just defined transfer operator, set $\boldsymbol{n}_p := \boldsymbol{n}^\Phi(p)$, and get the algebraic form of discrete non-penetration,

$$((\boldsymbol{u}_h^s)_p - (\boldsymbol{T}\boldsymbol{u}_h^m)_p) \cdot \boldsymbol{n}_p - g_p \leq 0, \quad \forall\, p \in \mathcal{N}_C^s, \tag{9}$$

where $\boldsymbol{g} = (g_p)_{p \in \mathcal{N}_C^s}$ denotes the weighted gap vector with

$$g_p := (\boldsymbol{D}^{-1}\boldsymbol{g}')_p \cdot \boldsymbol{n}_p, \quad (\boldsymbol{g}')_p := \left(\int_{\Gamma_C^s} \psi_p g \, d\boldsymbol{a} \right) \boldsymbol{n}_p, \quad p \in \mathcal{N}_C^s. \tag{10}$$

Note that in general (9) is not equivalent to (8) if $\boldsymbol{D}$ is not a diagonal matrix with positive entries. The latter can be achieved by using dual Lagrange multipliers

or mass lumping, see Section 3.3. Now, we can define a discrete approximation of the set of admissible displacements $\mathcal{K}$,

$$\mathcal{K}_h := \{\boldsymbol{v}_h \in \boldsymbol{X}_h |\ ((\boldsymbol{v}_h^s)_p - (\boldsymbol{T}\boldsymbol{v}_h^m)_p) \cdot \boldsymbol{n}_p - g_p \leq 0,\ \forall\, p \in \mathcal{N}_C^s\}\,,$$

and state the discrete variational problem: Find $\boldsymbol{u}_h \in \mathcal{K}_h$ so that

$$a(\boldsymbol{u}_h, \boldsymbol{v}_h - \boldsymbol{u}_h) \geq f(\boldsymbol{v}_h - \boldsymbol{u}_h), \quad \forall\, \boldsymbol{v}_h \in \mathcal{K}_h. \tag{11}$$

The solvability of the discrete problem (11) is again a classic result of convex analysis and follows as specified at the end of Section 2. The solution is unique if the discrete Dirichlet boundary on each body is sufficiently large, so that a discrete version of Korn's inequality holds. The discretization is indeed non-conforming. Since the weak coupling constraints generally cannot prevent a small penetration of the bodies, we have $\mathcal{K}_h \not\subset \mathcal{K}$.

3.2. Optimal error estimate. In this subsection, we outline how the weak coupling of the mortar method yields an optimal a priori estimate for the multi-body contact problem even in the case of non-matching meshes. The first-order convergence in the $\boldsymbol{H}^1$-norm we attain on each individual body by discretization with conforming linear finite elements is extended to the solution of the coupled system. For this purpose, we consider the bilinear form

$$b : H^{-\frac{1}{2}}(\Gamma_C^s) \times \boldsymbol{H}^{\frac{1}{2}}(\Gamma_C^s) \to \mathbb{R}, \quad b(\psi, \boldsymbol{v}) := \langle \psi, [v] \rangle,$$

where $\langle \cdot, \cdot \rangle$ denotes the duality pairing between $H^{-\frac{1}{2}}(\Gamma_C^s)$ and $H^{\frac{1}{2}}(\Gamma_C^s)$. We assume that $\boldsymbol{n}^\Phi$ and g are sufficiently smooth. Then, see [21, 28], the variational problem (11) is equivalent to the mixed formulation: Find $\boldsymbol{u}_h \in \boldsymbol{X}_h$ and $\mu_h \in M_h$ so that

$$\begin{array}{lcll} a(\boldsymbol{u}_h, \boldsymbol{v}_h) + b(\mu_h, \boldsymbol{v}_h) & = & f(\boldsymbol{v}_h), & \forall\, \boldsymbol{v}_h \in \boldsymbol{X}_h, \\ b(\psi_h, \boldsymbol{u}_h) & \leq & \langle \psi_h, g \rangle, & \forall\, \psi_h \in M_h. \end{array}$$

Let the two-dimensional meshes of the contact boundaries inherited from $\mathcal{T}^k$, $k \in \{m, s\}$, be quasi-uniform so that an inverse inequality holds. With the aid of an interpolation argument one shows the $H^{\frac{1}{2}}$-continuity of the mortar projection operator, see [6]. Hence, the following uniform inf-sup condition holds, which is well known from the theory of saddle point problems,

$$\inf_{\psi_h \in M_h} \sup_{\boldsymbol{v}_h \in \boldsymbol{X}_h} \frac{b(\psi_h, \boldsymbol{v}_h)}{||\psi_h||_{H^{-\frac{1}{2}}(\Gamma_C^s)} ||\boldsymbol{v}_h||_{\boldsymbol{X}}} \geq \beta,$$

with $\beta \neq \beta(h)$, see [4, 10, 44]. Then, under additional but mild assumptions on the regularity of the jump in normal direction and the boundary stresses as well as the shape of the actual contact boundary, one can show an a priori estimate of the form

$$||\boldsymbol{u} - \boldsymbol{u}_h||_{\boldsymbol{X}} + ||\mu - \mu_h||_{H^{-\frac{1}{2}}(\Gamma_C^s)} \leq C h^{\frac{1}{2}+\alpha} \sum_{k \in \{m,s\}} |\boldsymbol{u}^k|_{\boldsymbol{H}^{\frac{3}{2}+\alpha}(\Omega^k)},$$

see [12, 26], provided that $\boldsymbol{u}^k \in \boldsymbol{H}^{\frac{3}{2}+\alpha}(\Omega^k)$, $k \in \{m, s\}$, for all $\alpha \in (0, \frac{1}{2}]$. Without the additional assumptions it is still possible to show convergence of order up to $\frac{3}{4}$, see [5].

3.3. Modifications and remarks. In a flexible numerical simulation one does not only want to prescribe inequality constraints at contact interfaces but also to "glue" bodies with different material parameters, which shall be considered as permanently connected, at interior interfaces. The choice of a vector valued multiplier space $\boldsymbol{M}_h$ facilitates an integrative approach for these two purposes. Instead of enforcing the inequalities (9), at an interior interface we constrain the relative displacement in all spatial directions by

$$(\boldsymbol{u}_h^s)_p - (\boldsymbol{T}\boldsymbol{u}_h^m)_p = \boldsymbol{0}, \quad \forall\, p \in \mathcal{N}_C^s. \tag{12}$$

This is in fact the coupling originally suggested in [7], apart from the inclusion of the contact mapping $\boldsymbol{\Phi}$. Per constructionem the latter approach also copes with geometrically non-matching interfaces between such bodies, which usually emerge during the mesh-construction process of complex geometries. The iterative solver, a monotone multigrid method we present in Section 5, actually makes no difference between the two cases since both are solved by constrained energy minimization.

Moreover, the ansatz outlined before can easily be generalized to contact problems with friction and in particular our methods provide this opportunity, see [32]. In that case the tangential components of the Lagrange multipliers play the role of the scaled discrete tangential stresses. Since these stresses depend on the normal stresses and the relative tangential displacements nonlinearly via a friction law, e. g., according to Coulomb, new difficulties arise during the numerical solution process we do not consider in this paper. We rather refer to [25, 32, 38].

If we use dual Lagrange multipliers, see [44], which are characterized by the biorthogonality relation

$$\int_{\Gamma_C^s} \psi_p \lambda_q^s \, d\boldsymbol{a} = \delta_{pq} \int_{\Gamma_C^s} \lambda_q^s \, d\boldsymbol{a}, \quad \forall\, p, q \in \mathcal{N}_C^s, \tag{13}$$

the matrix $\boldsymbol{D}$ becomes diagonal and, hence, admits of a direct computation of its inverse. Otherwise $\boldsymbol{D}$ is a band matrix and a sparse linear system would have to be solved on Γ_C^s in order to compute the transfer operator $\boldsymbol{T}$. Unfortunately, the construction of dual multiplier spaces for surface meshes containing general convex quadrilaterals is nontrivial, see [19] for an approach taking into account that the transformation to the reference element is generally not affine.

Here, for simplicity, we choose the standard nodal basis functions on the slave side as multipliers, i. e. $\psi_p := \lambda_p^s$, $p \in \mathcal{N}_C^s$. Additionally, to avoid the computation of an inverse mass matrix on Γ_C^s that would necessarily have to be carried out and to retain the pointwise inequalities when multiplying with $\boldsymbol{D}^{-1}$ in (9), we lump the matrix $\boldsymbol{D}$,

$$d_{pq} \mapsto \delta_{pq} \left(\sum_{r \in \mathcal{N}_C^s} d_{rq} \right), \quad p, q \in \mathcal{N}_C^s.$$

Now the entries of $\boldsymbol{D}$ equal the term on the right hand side of (13), due to the fact that the basis of the Lagrange multiplier space forms a partition of unity. Another advantage of our choice is that no stabilization as in [18, 19] is necessary. The numerical studies in Section 6 will be evidence of this being a reasonable approach. Particularly, we draw an exemplary comparison of the dual multipliers on the one hand and the nodal multipliers with lumping on the other hand.

4. The discrete coupling operator. Although allowing for the straightforward computation of the master-slave coupling in the case of matching contact interfaces (but possibly non-matching meshes), mortar finite elements require substantial effort in implementation and additional analysis when complex geometries are involved. Therefore, previous numerical analyses, implementations, and experiments in context of domain decomposition as well as of contact problems predominantly deal with a simplified setting and impose a restriction of the form $\Gamma_C^m = \Gamma_C^s$, see, e. g., [5, 12, 22, 24, 38].

In this section, we focus on multi-body contact problems with geometrically non-matching contact boundaries and develop an efficient method to assemble the discrete coupling operator. A first idea for the handling of this more sophisticated case by projecting the mesh of the contact boundaries onto an explicitly given two-dimensional submanifold of $\mathbb{R}^3$ can be found in [15]. In [41, 42] the boundaries are projected onto a plane varying with the slave side, instead. Then, the coupling terms are computed by numerical integration on intersections of projected faces in this plane. Further possibilities are the automatic construction of an approximative contact mapping, see [33], or the usage of a priori known parametrizations of the contact boundaries, see [17, 18].

Here, we derive an algorithm, which assembles the discrete coupling between master and slave side from local information exclusively. We compute triangulated intersections of two respective faces in a locally adjusted projection plane but, unlike before, carry out the quadrature on the possibly warped slave side Γ_C^s directly. Our element-based approach does not use any parametrizations of the two-dimensional faces and is also suitable for isoparametric elements. After the derivation, in Subsection 4.2 we analyze the individual steps of the algorithm, specify details of the implementation, and compare our approach with previous ones.

4.1. Derivation of the assembly algorithm. Recall the definition of the discrete mortar transfer operator $\boldsymbol{T} := \boldsymbol{D}^{-1}\boldsymbol{B}$ via (6) and (7). Since the Lagrange multipliers are associated with the slave side Γ_C^s, the functions ψ_p and λ_q^m are defined on geometrically distinct subdomains and the expression (7) cannot be evaluated without further knowledge about the contact mapping $\boldsymbol{\Phi}$. To overcome this difficulty, we choose to compute the entries of the coupling matrices $\boldsymbol{B}$ and $\boldsymbol{D}$ by an algorithm motivated by [33, 41]. Our approach can be recognized as an approximation of $\boldsymbol{\Phi}$ by a composition of local projections and inverse projections. Incorporating the local variation of the area element, we expect our quadrature to reflect the integral over a warped slave side Γ_C^s very well. First, we justify our approach by a formal derivation of the algorithm with the idealized assumption that the contact mapping $\boldsymbol{\Phi}$ is completely known. Then, we see that the derived formula for the local contributions to the coupling terms only depends on few geometrical objects, which can easily be substituted by suitable discrete approximations to eliminate the appearance of the contact mapping.

Let $\mathcal{F}^m$ and $\mathcal{F}^s$ be the sets of master and slave faces, respectively. Only to ease the derivation of the algorithm, we assume a bounded set $U \subset \mathbb{R}^2$ and global parametrizations $\boldsymbol{\varphi}_k : U \to \Gamma_C^k$ of Γ_C^k, $k \in \{m, s\}$, to be given so that $\boldsymbol{\Phi} = \boldsymbol{\varphi}_m \circ \boldsymbol{\varphi}_s^{-1}$. This means that points on the contact boundaries which have the same preimages in the parameter domain U are possible contact partners. We point out that the parametrizations will shortly be replaced by suitable discrete and local versions, which are immediately computable from the geometric information already available in finite element programs. Hence, we neither dwell on the structures of $\boldsymbol{\varphi}_m$ and $\boldsymbol{\varphi}_s$ nor on

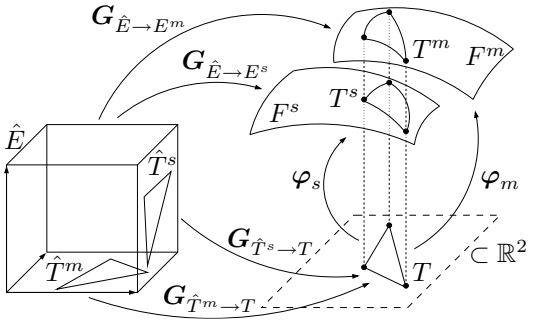

FIG. 1. *Derivation of the assembly algorithm for the coupling matrices.*

the question of their existence now and refer to [14] instead.

In the following, we denote the (three-dimensional) element from the mesh $\mathcal{T}^k$ belonging to the face F^k by E^k. We generically denote the respective reference element of E^m and E^s by $\hat{E}$. The coordinate transformation from $\hat{E}$ to E^k is called $\boldsymbol{G}_{\hat{E}\to E^k}$ and the affine transformation between two triangles T_1 and T_2 is $\boldsymbol{G}_{T_1\to T_2}$.

We use the decompositions of the contact boundaries into faces F^m and F^s induced by the meshes $\mathcal{T}^m$ and $\mathcal{T}^s$ and observe the fact that the set $\{\boldsymbol{\Phi}^{-1}(F^m)|\ F^m \in \mathcal{F}^m\}$ is a partition of the slave side Γ_C^s. In particular, for each slave face $F^s \in \mathcal{F}^s$ we have $\cup_{F^m\in\mathcal{F}^m}\left(F^s \cap (\boldsymbol{\varphi}_s \circ \boldsymbol{\varphi}_m^{-1})(F^m)\right) = F^s$. Then, integrating by substitution, we write formally,

$$
\begin{aligned}
b_{pq} &= \int_{\Gamma_C^s} \psi_p \cdot (\lambda_q^m \circ \boldsymbol{\Phi})\, d\boldsymbol{a} = \sum_{F^s\in\mathcal{F}^s} \left(\int_{F^s} \psi_p \cdot (\lambda_q^m \circ \boldsymbol{\varphi}_m \circ \boldsymbol{\varphi}_s^{-1})\, d\boldsymbol{a} \right) \\
&= \sum_{\substack{F^s\in\mathcal{F}^s \\ F^m\in\mathcal{F}^m}} \left(\int_{F^s\cap(\boldsymbol{\varphi}_s\circ\boldsymbol{\varphi}_m^{-1})(F^m)} \psi_p \cdot (\lambda_q^m \circ \boldsymbol{\varphi}_m \circ \boldsymbol{\varphi}_s^{-1})\, d\boldsymbol{a} \right) \\
&= \sum_{\substack{F^s\in\mathcal{F}^s \\ F^m\in\mathcal{F}^m}} \left(\int_{\boldsymbol{\varphi}_s^{-1}(F^s)\cap\boldsymbol{\varphi}_m^{-1}(F^m)} (\psi_p \circ \boldsymbol{\varphi}_s) \cdot (\lambda_q^m \circ \boldsymbol{\varphi}_m) \cdot |\det \boldsymbol{\nabla}\boldsymbol{\varphi}_s|\, d\boldsymbol{a} \right).
\end{aligned}
$$

We now assume that each intersection $\boldsymbol{\varphi}_s^{-1}(F^s) \cap \boldsymbol{\varphi}_m^{-1}(F^m) \subset \mathbb{R}^2$ can be divided into finitely many triangles, and for each triangle T we denote the corresponding triangles on the contact boundaries by $T^k := \boldsymbol{\varphi}_k(T)$, $k \in \{m, s\}$, see Figure 1 in case E^m and E^s are hexahedrons. Then, we transfer the triangles to the reference element with the inverses of the three-dimensional transformations, namely $\hat{T}^k := \boldsymbol{G}_{\hat{E}\to E^k}^{-1}(T^k)$. Now the two-dimensional affine transformations $\boldsymbol{G}_{\hat{T}^k\to T}$ from these triangles $\hat{T}^k$ to the triangle T can easily be computed. Hence, we have $\boldsymbol{\varphi}_k|_T \equiv \boldsymbol{G}_{\hat{E}\to E^k} \circ \boldsymbol{G}_{\hat{T}^k\to T}^{-1}$ and are in a position to continue the above formal calculation for the contribution of each

triangle T separately,

$$\int_T (\psi_p \circ \boldsymbol{\varphi}_s) \cdot (\lambda_q^m \circ \boldsymbol{\varphi}_m) \cdot |\det \boldsymbol{\nabla} \boldsymbol{\varphi}_s| \, d\boldsymbol{a} = \tag{14}$$

$$|\det \boldsymbol{\nabla} \boldsymbol{G}^{-1}_{\hat{T}^s \to T}| \int_T (\hat{\psi}_p \circ \boldsymbol{G}^{-1}_{\hat{T}^s \to T}) \cdot (\hat{\lambda}_q \circ \boldsymbol{G}^{-1}_{\hat{T}^m \to T}) \cdot |\det \boldsymbol{\nabla} \boldsymbol{G}_{\hat{E} \to E^s}(\boldsymbol{G}^{-1}_{\hat{T}^s \to T})| \, d\boldsymbol{a}.$$

At this we use the representation of the nodal basis functions via the shape functions on the reference element, $\psi_p \circ \boldsymbol{G}_{\hat{E} \to E^s} = \hat{\psi}_p$ and $\lambda_q^m \circ \boldsymbol{G}_{\hat{E} \to E^m} = \hat{\lambda}_q$. By abuse of notation $\boldsymbol{\nabla} \boldsymbol{G}_{\hat{E} \to E^s}$ stands for its restriction to the corresponding faces in the domain $\hat{E}$ and the codomain E^s, respectively. Thus, the exclusive use of the three-dimensional finite element transfomations supersedes the additional introduction of two-dimensional parametrizations of warped faces. Besides, we note that $|\det \boldsymbol{\nabla} \boldsymbol{G}^{-1}_{\hat{T}^s \to T}| = \frac{|\hat{T}^s|}{|T|}$ is constant because $\boldsymbol{G}_{\hat{T}^s \to T}$ is an affine mapping.

These considerations lead to the understanding that the entries b_{pq} of the coupling matrix $\boldsymbol{B}$ can be computed as a sum of integrals of the form (14) over triangles. This requires that suitable approximations of the parametrizations $\boldsymbol{\varphi}_k$ are known. In fact there is no need to establish any parametrizations explicitly. We only have to replace all triangles T, T^m, and T^s by approximating ones to allow for the evaluation of the right hand side of (14). For this purpose, we introduce the following algorithm. Firstly, the intersections and their triangulations are computed in a projection plane locally adjusted to the slave side. Secondly, the triangles T^m and T^s on the respective possible contact boundaries Γ_C^m and Γ_C^s are created by an inverse projection. Then, an appropriate quadrature formula can be applied on the respective reference elements directly.

Algorithm.

(A1) Build an octree data structure to determine which master and slave faces are "close" to each other.
(A2) Loop over all slave faces $F^s \in \mathcal{F}^s$.
  (B1) Loop over all master faces $F^m \in \mathcal{F}^m$.
    (C1) Only continue if F^m is "close" to F^s.
    (C2) Apply a Householder reflection H so that $H(\boldsymbol{n}^s) = \boldsymbol{e}_3$, where $\boldsymbol{n}^s$ is a suitably chosen outer normal of the current slave face.
    (C3) Compute $\tilde{F}^k$ as the convex hull of the corners of F^k projected onto the $\boldsymbol{e}_1\boldsymbol{e}_2$-plane, $k \in \{m, s\}$.
    (C4) Compute the intersection $\tilde{F} := \tilde{F}^m \cap \tilde{F}^s$ and a triangulation $\tilde{F} = \cup T_i$.
    (C5) Loop over all triangles T_i.
      (D1) Perform an inverse projection of the corners of T_i to get corresponding triangles T_i^m and T_i^s on the original faces F^m and F^s, respectively.
      (D2) Use the inverse of the transformation $\boldsymbol{G}_{\hat{E} \to E^k}$ to compute the triangle $\hat{T}_i^k$ on the reference element, $k \in \{m, s\}$.
      (D3) Use a two-dimensional quadrature formula to create weights ω_l and integration points $\boldsymbol{x}_l^m$ and $\boldsymbol{x}_l^s$ on the triangles $\hat{T}_i^m$ and $\hat{T}_i^s$, respectively.
      (D4) Set $\omega_l' := \omega_l \, |\det \boldsymbol{\nabla} \boldsymbol{G}_{\hat{E} \to E^s}(\boldsymbol{x}_l^s)| \, |\hat{T}_i^s|$.

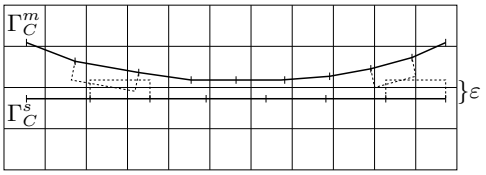

FIG. 2. *Layout of the octree.*

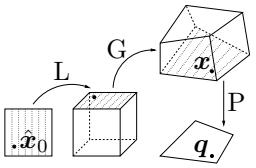

FIG. 3. *Inverse projection.*

(D5) Add the contribution of triangle T_i,

$$\begin{aligned} b_{pq} &\mapsto b_{pq} + \sum_l \omega_l' \hat{\psi}_p(\boldsymbol{x}_l^s)\hat{\lambda}_q(\boldsymbol{x}_l^m), \quad p \in \mathcal{N}_C^s, q \in \mathcal{N}_C^m, \\ d_{pq} &\mapsto d_{pq} + \sum_l \omega_l' \hat{\psi}_p(\boldsymbol{x}_l^s)\hat{\lambda}_q(\boldsymbol{x}_l^s), \quad p, q \in \mathcal{N}_C^s. \end{aligned} \tag{15}$$

(C6) End of loop over triangles T_i.
(B2) End of loop over master faces F^m.
(A3) End of loop over slave faces F^s.
(A4) Set $\boldsymbol{b}_{pq} := b_{pq}\, \boldsymbol{I}$ and $\boldsymbol{d}_{pq} := d_{pq}\, \boldsymbol{I}$.

Of course in the assembly of the contributions in step (D5) one only has to consider a shape function if $\operatorname{int}(\operatorname{supp}(\psi_p)) \cap F^s \neq \emptyset$ and in $(15)_1$ additionally $\operatorname{int}(\operatorname{supp}(\lambda_q^m)) \cap F^m \neq \emptyset$ and in $(15)_2$ additionally $\operatorname{int}(\operatorname{supp}(\lambda_q^s)) \cap F^s \neq \emptyset$, respectively.

4.2. Analysis of the algorithm. In this subsection we carry out a detailed analysis of the developed algorithm and show that it provides an efficient and effective method to assemble the weak coupling constraints. At the beginning we remark that an adaptation to a two-dimensional contact problem is easily achievable. Since we have specifically constructed the algorithm to overcome the difficulties of the more complex three-dimensional case, we only examine this setting.

Efficient structuring by octree. To ensure that the intersection computation in (C4) is only performed for reasonable choices of master and slave faces, we carry out a preprocessing step (A1) to distribute all faces to the leaves of an octree by their positions in three-dimensional space. The one-time creation of the octree is of complexity $\mathcal{O}(|\mathcal{N}_C| \cdot \log(|\mathcal{N}_C|))$. We refer to [1] for details on the implementation and in particular on the adaptivity of the octree structure. Then, in the following procedure only faces lying in the same leaf are considered "close" to each other. See Figure 2 for a simplified two-dimensional sketch.

On the one hand this method results in the optimal complexity $\mathcal{O}(|\mathcal{N}_C^s|)$ of the actual assembly routine and on the other hand it facilitates the separation of faces which cannot get into contact because of geometrical reasons. Note that the detection of intersection candidates is only well posed if we "blow up" the two-dimensional faces by an $\varepsilon > 0$ in positive normal direction. Otherwise two faces could be separated by the octree even though they are close to each other. Naturally, the parameters for the design of the octree have to be chosen problem dependent, particularly the parameter ε should be a little greater than half of the maximal initial gap g and the minimal leaf diameter a little greater than 2ε. A simple test wether the settings have led to a correct assembly of the mortar transfer operator is the computation of its line totals we explain at the end of the section. In the case of three or more bodies we can choose to build several octrees if the optimal parameters vary strongly with the diverse contact boundaries.

Projections instead of parametrizations. By the application of the Householder reflection H in (C2) we transform the configuration so that each individual slave face F^s roughly lies in a plane parallel to the $\boldsymbol{e}_1\boldsymbol{e}_2$-plane. This can be achieved if we choose $\boldsymbol{n}^s$ as the normal at the barycenter. Let $F_1^m, \dots, F_n^m$ denote the master faces close to F^s determined by the octree. Then, for properly chosen octree parameters, the projection onto the $\boldsymbol{e}_1\boldsymbol{e}_2$-plane maps each master face F_i^m, their union $\cup F_i^m$, and the current slave face F^s bijectively onto its respective image. Further, their inverse mappings can be regarded as local parametrizations $\boldsymbol{\varphi}_{F_1^m[F^s]}, \dots, \boldsymbol{\varphi}_{F_n^m[F^s]}$ of the master faces and $\boldsymbol{\varphi}_{F^s}$ of the slave face, see Figure 4. Note that the parametrization $\boldsymbol{\varphi}_{F_i^m[F^s]}$ of the master face F_i^m depends on the current slave face F^s by the choice of the projection plane or $\boldsymbol{n}^s$. We indicate this dependency by the subscript $_{[F^s]}$.

We compose these locally defined mappings to a global approximation $\boldsymbol{\Phi}_h$ of the contact mapping. This mapping $\boldsymbol{\Phi}_h := \boldsymbol{\varphi}_m \circ \boldsymbol{\varphi}_s^{-1} : \Gamma_C^s \to \Gamma_C^m$ is defined piecewisely by

$$\left(\boldsymbol{\varphi}_m \circ \boldsymbol{\varphi}_s^{-1}\right)(\boldsymbol{x}) := \boldsymbol{\varphi}_{F_i^m[F^s]}\left(\boldsymbol{\varphi}_{F^s}^{-1}(\boldsymbol{x})\right), \text{ if } \boldsymbol{x} \in F^s \text{ and } \boldsymbol{\varphi}_{F^s}^{-1}(\boldsymbol{x}) \in \boldsymbol{\varphi}_{F_i^m[F^s]}^{-1}(F_i^m). \quad (16)$$

It is well defined, since (because of the bijectivity discussed above) the projection of the master faces is a decomposition of the projection of the slave face and, hence, for each $\boldsymbol{x} \in F^s$ there is a unique master face F_i^m, so that $\boldsymbol{\varphi}_{F^s}^{-1}(\boldsymbol{x}) \in \boldsymbol{\varphi}_{F_i^m[F^s]}^{-1}(F_i^m)$. In other words, the projection of the point $\boldsymbol{x}$ lies in the projection of precisely one master face.

Although in general the piecewisely defined composition $\boldsymbol{\varphi}_m \circ \boldsymbol{\varphi}_s^{-1}$ does not equal $\boldsymbol{\Phi}$, it is closely related to an a priori approximation of the unknown contact mapping by normal projection as in [33]. Because of the potential discontinuity of $\boldsymbol{\Phi}_h$ across the edges of the slave faces we cannot even expect its local bijectivity, which is guaranteed on each single face F^s by the definition (16), to be conserved by the composition. See Figure 5 for a situation with

$$\lim_{\boldsymbol{x} \in F_l^s,\, \boldsymbol{x} \to \boldsymbol{x}^s} \boldsymbol{\Phi}_h(\boldsymbol{x}) = \boldsymbol{x}_l^m \neq \boldsymbol{x}_r^m = \lim_{\boldsymbol{x} \in F_r^s,\, \boldsymbol{x} \to \boldsymbol{x}^s} \boldsymbol{\Phi}_h(\boldsymbol{x}).$$

But, within the kinematically linear framework, coupling and constraints only in normal direction are a common and appropriate method of approximation. The numerical studies in this paper will demonstrate its effectiveness later on.

The exact effect of the approximative assembly of the coupling conditions on the error estimates from the previous section has not been successfully analyzed yet. A first attempt for a similar problem in two dimensions and under the additional restriction that $\Gamma_C = \overline{\Omega}^m \cap \overline{\Omega}^s$ can be found in [17, 18] via a perturbation analysis for a blending element discretization.

Influence of quadrature formulas. So far we have seen that the computation of the entries of the coupling matrix $\boldsymbol{B}$ can be recognized as an elaborate construction of an approximate contact mapping $\boldsymbol{\Phi}_h$ and subsequent numerical integration of the terms $\int_{\Gamma_C^s} \psi_p \cdot (\lambda_q^m \circ \boldsymbol{\Phi}_h)\, d\boldsymbol{a}$ in step (D5). Since, in general, for warped contact boundaries $\boldsymbol{\Phi}_h$ is no polynomial, a quadrature rule does not necessarily reflect the integral exactly. Thus, an additional consistency error occurs, which we keep small by using enough integration points.

A rigorous analysis of this error due to inexact integration of the constraints cannot be achieved easily. But a similar problem arises for the mortar method in case of a linear problem with geometrically matching interfaces if a quadrature rule

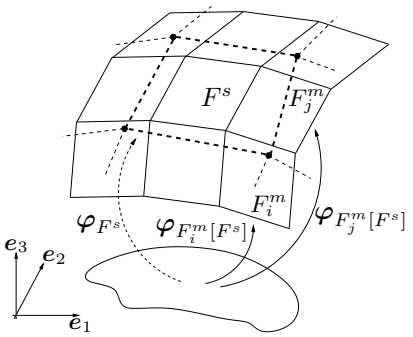

FIG. 4. *Approximation of the contact mapping.*

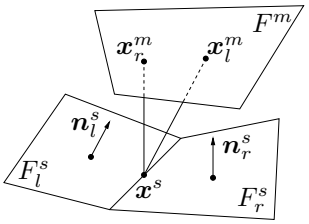

FIG. 5. *Potential discontinuity.*

is used which is only based on the triangulation either of the master or of the slave side, see, e. g., [16, 40]. Numerical examples in two and three dimensions exhibit that this omission of an adequate intersection computation has a negative effect on the discretization error. The available proposals how to preserve the optimality of the method by a Petrov-Galerkin approach, cf. [40], or an additional projection onto a discrete auxiliary space, in which the quadrature can more easily be carried out, cf. [16], cannot be directly transferred to our situation.

Intersection computation by the quickhull algorithm. For the computation of the intersection $\tilde{F}^m \cap \tilde{F}^s$ in step (C4) we use the quickhull algorithm QHULL implemented by Barber et al. [2]. Actually, a Delaunay triangulation of the intersection is computed, which we anticipate to minimize roundoff errors for the quadrature on the resulting triangles. QHULL is a flexible and efficient toolbox for several operations on convex hulls in arbitrary dimension and it also copes with degeneracies coming from imprecise data. The basic ingredient is the representation of a convex hull as intersection of several halfspaces each given as oriented hyperplane.

As additional input the algorithm needs a point which is a priori known to lie within the intersection. We compute such an interior point by a modified simplex algorithm particularly detecting wether an intersection is empty. Naturally, in our application (intersection of two faces) only small problems occur.

The description of the computation of the projection $\tilde{F}^k$ as convex hull of the projected corners in (C3), which at first sight seems to be unnecessarily involved, has been chosen for two reasons. On the one hand it is closer to the actual implementation whereas on the other hand it allows for the direct generalization of the algorithm to isoparametric elements of higher order. In that case the edges of the faces $\tilde{F}^k$ can be curvilinear. However, the edges of the triangles T^k are generally curvilinear even in the case of bilinear quadrangular faces.

Stable inverse projection. Using elements with quadrangular faces we cannot expect the transformation G from the reference element to an element E to be affine in general. But instead of assuming some extra parametrization of non-planar faces in three-dimensional space to be given, we propose an inverse projection, which only relies on the geometric information already available in finite element programs.

Given a corner $\boldsymbol{q} \in \mathbb{R}^2$ of a triangle in the $\boldsymbol{e}_1\boldsymbol{e}_2$-plane we projected onto in step (C3), in step (D1) we have to compute the corresponding point $\boldsymbol{x} \in \mathbb{R}^3$ on the master or slave face F. If F is a triangle, $\boldsymbol{x}$ is determined as the solution of a linear equation and can be computed immediately. So we only consider the case of F being

a quadrangle.

The inverse projection is essentially realized by means of a Newton iteration to find the appropriate root of the function

$$R : [0,1]^2 \to \mathbb{R}^2, \quad R(\hat{\boldsymbol{x}}) := (P \circ H \circ G \circ L)(\hat{\boldsymbol{x}}) - \boldsymbol{q},$$

with $\hat{\boldsymbol{x}}$ a point on the two-dimensional unit square, L the map to the respective face of the three-dimensional reference element (cube, pyramid, or prism), $H = H(\boldsymbol{n}^s)$ the Householder reflection used in step (C2), and P the projection onto the $\boldsymbol{e}_1\boldsymbol{e}_2$-plane. Then, the root $\hat{\boldsymbol{x}}_0$ of R yields the desired point via $\boldsymbol{x} = (G \circ L)(\hat{\boldsymbol{x}}_0)$, see Figure 3 in case of a hexahedral element and $H = \mathbf{id}$. Using the solution of an approximating linear equation as initial value, we observe good convergence behavior of the iteration and therefore compute the points at low cost. Such a linear system can be obtained by, e. g., roughly subdividing the quadrangle into two triangles.

Another approach is chosen in [41]. There, the quadrature is carried out on planar triangles in the intersection. For the evaluation of the basis functions each integration point is individually transferred to the original faces by normal projection. One could also use local parametrizations of the faces, see [42].

Balance of forces. For each given discrete multiplier $\boldsymbol{\psi}_h \in \boldsymbol{M}_h$ we require the total induced interface forces on the opposite contact boundaries to have equal norm and reverse sign. For dynamic problems this condition corresponds to the conservation of momentum, see, e. g., [41]. This directly follows from Newton's third law. The relevant forces can formally be written as integrals over Γ_C^m and Γ_C^s, respectively, which read as $\boldsymbol{\psi}_h^T \boldsymbol{B}\mathbf{1}$ and $\boldsymbol{\psi}_h^T \boldsymbol{D}\mathbf{1}$ in the discrete setting. Therefore, the requirement of force balance is equivalent to the following equation to hold for every slave node p,

$$\sum_{q \in \mathcal{N}_C^s} d_{pq} - \sum_{r \in \mathcal{N}_C^m} b_{pr} = 0, \quad \forall\, p \in \mathcal{N}_C^s. \tag{17}$$

We verify equation (17) by considering the contribution of each triangle T_i separately and using the fact that the nodal basis functions of the Lagrangian finite elements form a partition of unity:

$$\begin{aligned} \sum_{q \in \mathcal{N}_C^s} d_{pq} - \sum_{r \in \mathcal{N}_C^m} b_{pr} &= \sum_{T_i} \left(\sum_q \sum_l \omega_l' \psi_p(\boldsymbol{x}_l^s) \lambda_q^s(\boldsymbol{x}_l^s) - \sum_r \sum_l \omega_l' \psi_p(\boldsymbol{x}_l^s) \lambda_r^m(\boldsymbol{x}_l^m) \right) \\ &= \sum_{T_i} \left(\sum_l \omega_l' \psi_p(\boldsymbol{x}_l^s) - \sum_l \omega_l' \psi_p(\boldsymbol{x}_l^s) \right) = 0. \end{aligned}$$

Note that for the respective computation of b_{pq} and d_{pq} in (15) we use the same partition into triangles and the same quadrature points $\boldsymbol{x}_l^s$ on the slave side to guarantee (17) to hold exactly, i. e. up to machine accuracy. However, numerical studies show a very good balance of forces if the coupling on the slave side is assembled independently but using a sufficient number of integration points.

Having assembled the mortar transfer operator $\boldsymbol{T}$ as outlined before, we can use the computation of the line totals of $\boldsymbol{T}$ in (17) as a test for the admissibility of the applied octree parameters. If this equation does not hold for every node $p \in \mathcal{N}_C^s$ except for roundoff errors, the parameters have to be chosen less restrictively.

5. Minimization with linearized constraints. As solution algorithm for the nonlinear multi-body contact problem discretized by mortar finite elements we apply

a monotone multigrid method to be briefly presented in this section. Elsewhere, methods from mathematical optimization are frequently used, see [36, 46] for an overview. Penalty methods, see, e. g., [22], employ a penetration parameter to smooth out the non-differentiability in the energy functional to be minimized, which evolves due to the constraints. Moreover, one finds augmented Lagrangian approaches, see, e. g., [37, 42], which directly utilize the underlying saddle point structure of the problem. If active set strategies are used instead, the discrete contact boundary is iterated and a sequence of linear problems with fixed contact boundary is solved, see [25, 27]. Furthermore, the problem can be solved by a nonlinear Dirichlet-Neumann algorithm derived in [15, 34], in which the information exchange between the two subproblems can be efficiently realized by the discrete mortar transfer operator and its adjoint mapping.

5.1. Monotone multigrid method. To ease the notation, we decompose the set of nodes $\mathcal{N} := \mathcal{N}^m \cup \mathcal{N}^s$ into the master nodes $\mathcal{M} := \mathcal{N}_C^m$, the slave nodes $\mathcal{S} := \mathcal{N}_C^s$, and the interior nodes $\mathcal{I} := \mathcal{N} \setminus (\mathcal{M} \cup \mathcal{S})$. Thus, the nodal basis of the unconstrained product space $\boldsymbol{X}_h$ is $\boldsymbol{\lambda} = (\boldsymbol{\lambda}_\mathcal{I}, \boldsymbol{\lambda}_\mathcal{M}, \boldsymbol{\lambda}_\mathcal{S})^T$. As usual, a finite element function $\boldsymbol{v}_h \in \boldsymbol{X}_h$ is identified with the vector $(\boldsymbol{v}_\mathcal{I}, \boldsymbol{v}_\mathcal{M}, \boldsymbol{v}_\mathcal{S})^T$.

We notice that the realization of the discrete contact constraints (9) requires the evaluation of the discrete jump $\boldsymbol{v}_\mathcal{S} - \boldsymbol{T}\boldsymbol{v}_\mathcal{M}$. To obtain a formulation in which these discrete relative displacements appear directly, we follow [45] and define a new basis $\boldsymbol{\lambda}'$ by the local transformation

$$\boldsymbol{\lambda}' := \begin{pmatrix} \boldsymbol{\lambda}'_\mathcal{I} \\ \boldsymbol{\lambda}'_\mathcal{M} \\ \boldsymbol{\lambda}'_\mathcal{S} \end{pmatrix} := \begin{pmatrix} \boldsymbol{I} & \boldsymbol{0} & \boldsymbol{0} \\ \boldsymbol{0} & \boldsymbol{I} & \boldsymbol{T}^T \\ \boldsymbol{0} & \boldsymbol{0} & \boldsymbol{I} \end{pmatrix} \begin{pmatrix} \boldsymbol{\lambda}_\mathcal{I} \\ \boldsymbol{\lambda}_\mathcal{M} \\ \boldsymbol{\lambda}_\mathcal{S} \end{pmatrix} =: \boldsymbol{Q}\boldsymbol{\lambda}.$$

Then, $(\boldsymbol{\lambda}'_\mathcal{I}, \boldsymbol{\lambda}'_\mathcal{M})^T$ is a basis of the constrained product space

$$\boldsymbol{V}_h := \{\boldsymbol{v}_h \in \boldsymbol{X}_h |\ (\boldsymbol{v}_\mathcal{S})_p - (\boldsymbol{T}\boldsymbol{v}_\mathcal{M})_p = \boldsymbol{0},\ \forall\, p \in \mathcal{S}\}\,,$$

whereas $\boldsymbol{\lambda}'_\mathcal{S}$ spans the space of relative displacements. Therefore, the discrete nonpenetration condition is satisfied iff

$$(\boldsymbol{v}'_h)_p \cdot \boldsymbol{n}_p - g_p \leq 0, \quad \forall\, p \in \mathcal{S}, \tag{18}$$

so that in the modified basis the multi-body contact problem has the algebraic structure of a one-sided obstacle problem.

Now, after modifying the stiffness matrix and the right hand side according to the transformation $\boldsymbol{Q}$, we solve the nonlinear system by a monotone multigrid method developed in [30, 31] for Signorini's problem. This iterative procedure can be recognized as a multilevel energy minimization by the combination of a multigrid method and a nonlinear block Gauß-Seidel smoother. Neither regularization nor an outer iteration are necessary to gain global convergence. Under convenient premises the discrete contact boundary is detected after finitely many steps and the iteration degenerates into a linear subspace correction method. Its efficiency is obtained from the optimal complexity of each step of the iteration.

The usage of a vector valued multiplier space $\boldsymbol{M}_h$ in Section 3 allows for the enforcement of constraints in every direction, if necessary with an additional orthogonal basis transformation. For the frictionless contact problem, at the nodes in $\mathcal{S}$ pointwise, i. e. linearized constraints for the relative displacement in positive normal

direction are prescribed according to (18). For this purpose, in the assembly of the weighted gap vector $\boldsymbol{g} = (g_p)_{p\in\mathcal{S}}$ via numerical quadrature of the expression (10), we approximate the gap function g at an integration point $\boldsymbol{x}^s \in \Gamma_C^s$ by the distance to the master side along $\boldsymbol{n}^s(\boldsymbol{x}^s)$. However, for the simulation of "glued" bodies, which prohibit any relative displacement across the interior interface Γ_C, all upper and lower obstacles will be set to 0, see (12). For the extension to multi-body contact with Coulomb friction we refer to [32].

Although the solution algorithm does not use Lagrange multipliers explicitly, the occurring discrete boundary stresses can be computed from the linear residual via a local postprocessing step.

5.2. Handling of complex geometries. All methods presented in this paper have been implemented in the framework of the finite element toolbox UG ("unstructured grids"), see [3]. For the monotone multigrid method we use OBSLIB++, which is an extension of the implementation extensively described in [31]. On the coarse mesh we use the direct solver PARDISO ("parallel sparse direct solver"), see [43]. For the assembly of the discrete coupling operator derived in Section 4, a new toolbox CUTLIB has been created by one of the authors in [13] using [1, 2].

The implementation of a flexible data parser allows for the import of arbitrarily many bodies with unstructured volume meshes consisting of tetrahedrons, hexahedrons, pyramids, and prisms. This has been done as an extension of the EXODUS II format described in [20].

To facilitate realistic simulations, in which the complex geometries generally can be resolved by very fine meshes only, we also use parallel computing. If one guarantees that for a slave face each process is provided information about every master face which is close-by in terms of the octree, basic parallelization is implemented. We employ a sparse solver on the coarse mesh to efficiently solve the systems arising from quite fine meshes and, thus, contribute to the stability of the multigrid method.

5.3. Large deformation contact. In case of large deformations and nonlinear material behavior, the energy functional $\mathcal{J}$ becomes non-convex. Besides, a linearization of the contact conditions as in (2), (3) does not accurately approximate the exact geometric non-penetration condition. If the resulting non-convex minimization problem is solved by an SQP method applying the above multigrid method to the constrained quadratic subproblems, one has to incorporate the discrete coupling operator into the outer iteration. Since the local coupling is only reasonable for small deformations, this could imply additional box constraints in each SQP step and, thus, affect convergence. In a very similar manner, the time step size in a dynamic simulation should be subject to an additional constraint preventing too large deformations during one step. Naturally, these difficulties arise in the contact case but not in the "gluing" case.

6. Numerical results. In this section, we illustrate the effectivity of the methods developed in this paper by various examples. First of all, the validity of the error estimates from Section 3.2 in the numerical practice is verified. Then, we demonstrate that the coupling by means of the discrete mortar transfer operator performs very well in diverse geometrical situations and examine the occuring discrete boundary stresses. Even though the local shape of master and slave side and, especially, of the actual contact zone varies, the methods from Section 4 yield a discrete solution of the multi-body contact problem with smooth contact stresses and optimal convergence.

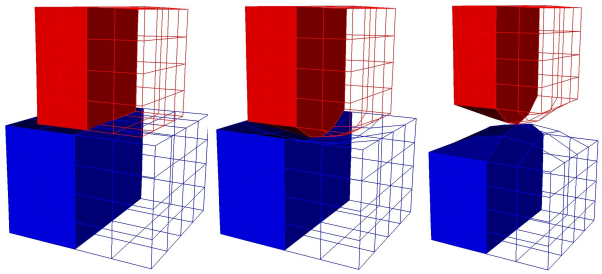

FIG. 6. *Meshes on level 2 for the model problems (a) to (c).*

l	# slave dof	# dof
0	12	48
1	27	162
2	75	750
3	243	4,374
4	867	29,478
5	3,267	215,622
6	12,675	1,647,750

FIG. 7. *Mesh hierarchy.*

6.1. Model problems. We consider three model problems, (a) to (c). Each geometrical configuration is composed of two bodies arranged on top of each other in $\boldsymbol{e}_3$-direction, see Figure 6. The upper body (red) is always generated from the cube $(0,1) \times (0,1) \times (1,2)$. In (b) we move it by 0.0625 and in (c) by 0.5 in $\boldsymbol{e}_3$-direction, respectively. The basic structure of the lower body (blue) is the cuboid $(-0.2,1.2) \times (-0.2,1.2) \times (0,1)$. Let every face not explicitly defined be described by the bilinear interpolation between the associated corners. In (b) and (c), let the $\boldsymbol{e}_3$-coordinate of the lower face of the cube and the upper face of the cuboid be given by a parametrization

$$\alpha\xi_1(1-\xi_1)\xi_2(1-\xi_2)+\beta \tag{19}$$

over the respective flat face in local coordinates $\boldsymbol{\xi} = (\xi_1, \xi_2) \in [0,1]^2$. In (b) we choose $\alpha = -3$, $\beta = 1.0625$ for the cube and $\alpha = -2$, $\beta = 1$ for the cuboid; in (c) we set $\alpha = -4$, $\beta = 1.5$ for the cube and $\alpha = 4$, $\beta = 1$ for the cuboid.

In each example we use the mesh consisting of two trilinear hexahedral elements with the 16 corners as stated above as starting point. Then, we create a mesh hierarchy by repeated uniform refinement, so that $h_l \approx h_{l-1}/2$, $l \geq 1$, where h_l is the mesh size on level l. We choose the lower boundary of the upper body to be the slave side Γ_C^s and the upper boundary of the lower body to be the master side Γ_C^m, respectively. See Figure 7 for the distribution of the degrees of freedom.

To compare the behavior of the discrete transfer operator in the different geometrical situations, we first prescribe Dirichlet boundary values for the displacements of $(0,0,-0.05)$ at the upper boundary of the upper body and of $(0,0,0.05)$ at the lower boundary of the lower body. At the remaining parts of the boundaries we have homogeneous Neumann boundary conditions. The unphysically large boundary conditions are chosen to emphasize the robustness of our method. We assume linear elastic material behavior and set E =10,000 MPa and $\nu = 0.3$. Since, indeed, the convergence of iterative solvers and the constants in the discretization error estimates depend on the material parameters, but not the quality of the information transfer itself, we do not carry out studies concerning the robustness of the method against variations in E or ν, here.

Now, on each level $l \geq 1$, we approximate the discrete solution $\boldsymbol{u}_{h_l}$ by $\tilde{\boldsymbol{u}}_{h_l}$ such that for the estimated algebraic error we have $||\tilde{\boldsymbol{u}}_{h_l} - \boldsymbol{u}_{h_l}||_{\boldsymbol{X}} \leq 10^{-10}$. Because no analytic solutions are available, we use the solution $\boldsymbol{u}_{h_6}$ computed on level 6 as reference solution $\boldsymbol{u}_{\text{ref}}$ to measure the discretization error in the $\boldsymbol{L}^2$-norm $||\cdot||_{\boldsymbol{L}^2(\Omega)}$ and the broken $\boldsymbol{H}^1$-norm $||\cdot||_{\boldsymbol{X}}$, respectively.

In example (a) all slave nodes belong to the discrete contact boundary. Figure 8 (left) shows the distribution of the von Mises equivalent stresses σ_{v} on a cut through

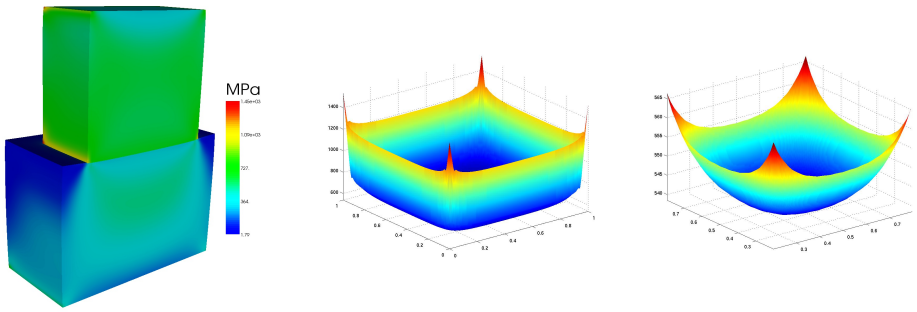

FIG. 8. *Problem (a): Cut through deformed configuration with von Mises stresses (left); normal stresses at complete contact boundary (center) and zoom around* $\boldsymbol{\xi} = (0.5, 0.5)$ *(right).*

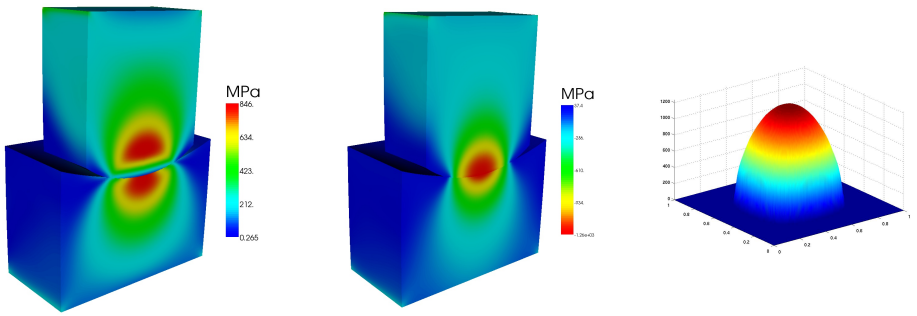

FIG. 9. *Problem (b): Cut through deformed configuration with von Mises stresses (left) and* σ_{33} *(center), respectively; normal stresses at complete contact boundary (right).*

the deformed configuration. The computed Lagrange multiplier μ_{ref}, which is the negative of the scaled normal stresses at the contact boundary, is depicted in the center. The von Mises stresses as well as the contact stresses increase rapidly towards the boundary of the actual contact zone. Nevertheless, as can be seen in the zoom around the center $\boldsymbol{\xi} = (0.5, 0.5)$ in the right picture of Figure 8, the stresses in the interior of the contact boundary are very well represented and show a smooth behavior.

In the examples with warped faces the discrete contact boundaries are smaller. On level 6 it contains 1,245 nodes in (b) and 429 nodes in (c), respectively. We note that we do not use the parametrizations of the contact boundaries during the assembly of the weighted gap vector $\boldsymbol{g}$ but proceed as in the general case mentioned in Section 5.1, instead.

For the problem (b), Figure 9 shows σ_{v} (left) as well as the component σ_{33} of $\boldsymbol{\sigma}(\boldsymbol{u})$ (center) on a cut through the deformed configuration. The broad paraboloid of the contact stresses is depicted on the right hand side. While the norm of the stress component σ_{33} becomes maximal at the contact boundaries, the maxima of σ_{v} are located inside the two bodies. This results from the fact that at the surface the shear stresses appear to be very small and the material is almost exclusively loaded by pure pressure.

In example (c) the paraboloid formed by the scaled normal stresses, which develops at the smaller actual contact zone, is considerably steeper than in example (b). See Figure 10 for the von Mises stresses (left) and the multiplier (center and right). Even so, the discrete normal stresses are smooth everywhere as can be seen in the

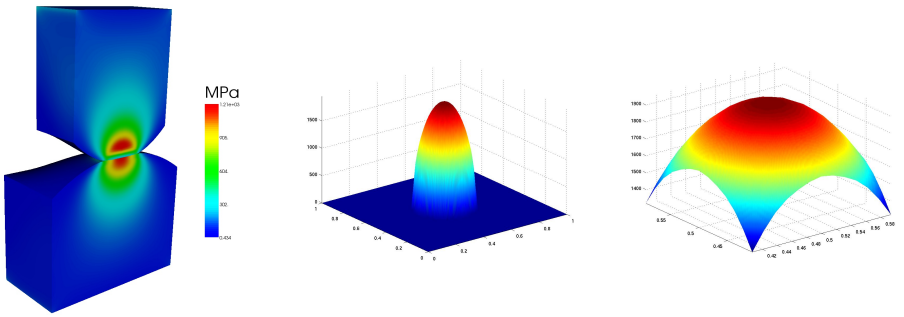

FIG. 10. *Problem (c): Cut through deformed configuration with von Mises stresses (left); normal stresses at complete contact boundary (center) and zoom around* $\boldsymbol{\xi} = (0.5, 0.5)$ *(right).*

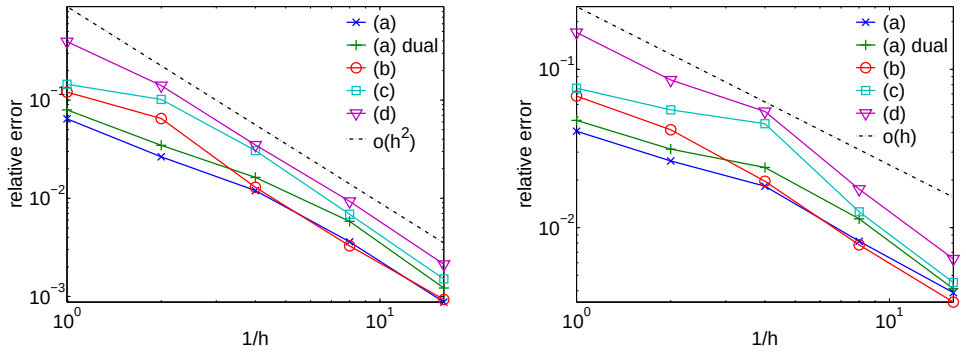

FIG. 11. *Relative discretization error in* $\boldsymbol{L}^2$*-norm (left) and broken* $\boldsymbol{H}^1$*-norm (right), respectively.*

zoomed picture on the right hand side.

Now, we examine the reduction of the discretization error by uniform refinement. For this purpose, we measure the relative $\boldsymbol{L}^2$-error as well as the relative broken $\boldsymbol{H}^1$-error with respect to the reference solution $\boldsymbol{u}_{\mathrm{ref}}$. If the exact solution is sufficiently smooth, we expect asymptotic convergence of order 2 and 1, respectively. The error decline we found in our experiments is depicted in Figure 11. Although it is quite unclear whether the regularity requirements hold for the considered contact problems, the data indicates asymptotically optimal convergence. A comparison of the nodal multipliers with lumping of the matrix $\boldsymbol{D}$ on the one hand with the dual multipliers on the other hand, which is carried out for example (a) only, shows no qualitative difference as well.

6.2. Wavy contact boundary. Let us consider another example, (d), with a more complicated, namely wavy possible contact boundary, see Figure 12 (left) for the mesh on level 4 of the reference configuration. For the construction of the two bodies, we use the same objects as before. We move the cube (red) by 0.1875 in $\boldsymbol{e}_3$-direction and apply the parametrization (19) with $\alpha = -3$ und $\beta = 1.1875$ to its lower face. The upper face of the cuboid (blue) obtains its wavy shape by the following composite

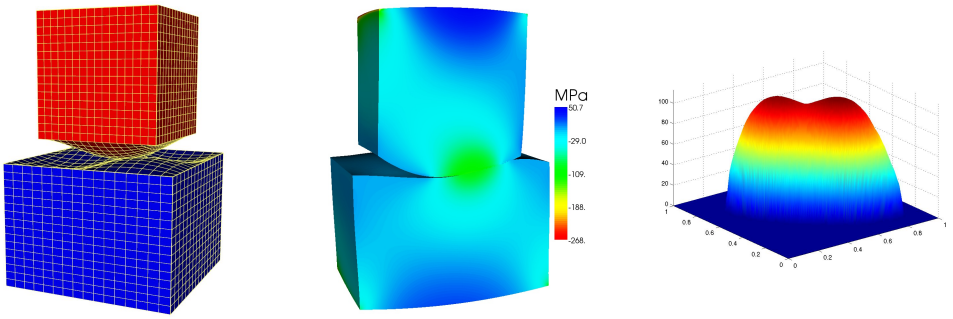

FIG. 12. *Problem (d): Mesh on level 4 (left); cut through deformed configuration with σ_{33} (center); normal stresses at complete contact boundary (right).*

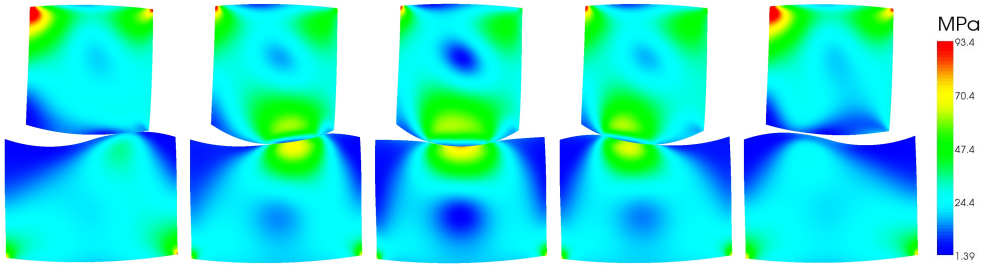

FIG. 13. *Problem (d): Cuts ($\boldsymbol{e}_1\boldsymbol{e}_3$-plane) through deformed configuration with von Mises stresses for $\boldsymbol{e}_2$-axis intercepts 0.1, 0.3, 0.5, 0.7, and 0.9 (from left to right).*

parametrization,

$$\begin{cases} -4\xi_1(1-2\xi_1)\xi_2(1-2\xi_2)+1, & \text{if } \boldsymbol{\xi} \in [0,0.5)\times[0,0.5)\,, \\ 8\xi_1(1-2\xi_1)(\xi_2-0.5)(1-\xi_2)+1, & \text{if } \boldsymbol{\xi} \in [0,0.5)\times[0.5,1]\,, \\ 8(\xi_1-0.5)(1-\xi_1)\xi_2(1-2\xi_2)+1, & \text{if } \boldsymbol{\xi} \in [0.5,1]\times[0,0.5)\,, \\ -16(\xi_1-0.5)(1-\xi_1)(\xi_2-0.5)(1-\xi_2)+1, & \text{if } \boldsymbol{\xi} \in [0.5,1]\times[0.5,1]\,. \end{cases}$$

For the materials we choose $E = 500$ MPa and $\nu = 0.2$ for the cuboid with the wavy potential contact boundary and $E = 1,000$ MPa and $\nu = 0.46$ for the cube with the bulge. At a point (x_1, x_2, x_3) on the lower face of the lower body and the upper face of the upper body, respectively, we set the positive or negative Dirichlet values

$$\big(0,\ 0,\ \pm\big(0.1(x_1-0.5)^2+0.1(x_2-0.5)^2+0.02(x_2-0.5)+0.03\big)\big)$$

for the displacements. Besides, we prescribe Neumann boundary values $(5, 0, -15)$ at the face of the upper body with $x_1 = 1$, i. e. "at the face to the right", and assume homogeneous Neumann boundary conditions elsewhere.

In Figure 12 (center) we have displayed σ_{33} on a cut through the deformed configuration. On the right hand side one sees the contact stresses, which form a union of two paraboloids of different height and width. Figure 13 shows the von Mises stresses σ_{v} on cuts parallel to the $\boldsymbol{e}_1\boldsymbol{e}_3$-plane for different $\boldsymbol{e}_2$-axis intercepts, namely from left to right 0.1, 0.3, 0.5, 0.7, and 0.9, in each case through the deformed configuration. Considering this sequence we notice that, because of the wavy shape of the master side and the design of the boundary values, the form of the actual contact boundary varies notably. In spite of the variations in the local shape and especially in the curvature and the initial gap of the two surfaces, we get a reasonable discrete solution

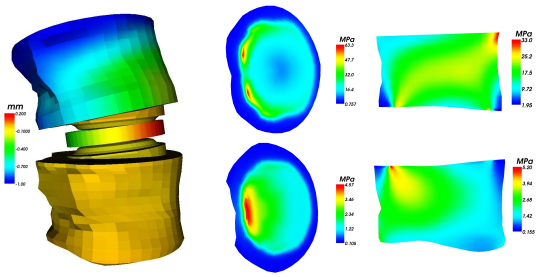

FIG. 14. *Vertebrae with implant: deformed configuration with displacements in $\boldsymbol{e}_3$-direction (left); lower/upper endplate of L4/L5 (center) and cut through L4/L5 (right), each with von Mises stresses.*

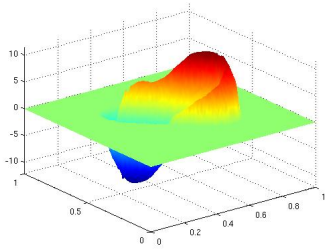

FIG. 15. *Contact problem with Coulomb friction for geometry (d): tangential stresses (component $\boldsymbol{\sigma}_t \cdot \boldsymbol{e}_1$) at complete contact boundary.*

using our discrete transfer operator. Locally this accounts for the smoothness of the contact stresses, while globally it yields smooth equivalent stresses. The plot indicating optimal convergence of the method in this more sophisticated case can, again, be found in Figure 11.

6.3. Gluing and friction. In this subsection, we demonstrate the flexibility and efficiency of our discretization as well as of the iterative solver by further examples. As a start, we consider a biomechanical application with a complex geometry, where both types of interface conditions, equality and inequality constraints, are necessary. Some numerical results regarding a model of the vertebral segment L4-L5 of the human lumbar spine with a CHARITÉ artificial disc, which has been implanted instead of the spinal disc, are depicted in Figure 14. Assuming that complete osseointegration of the implant has already taken place, we prescribe "gluing" conditions at the non-matching interfaces between bone and implant and contact conditions at the interfaces between its mobile polyethylen core and the metal plates, respectively. Then, for the loading case of axial compression, Figure 14 (left) shows the component $\boldsymbol{u}_3$ of the resulting displacements. In the center of the Figure one can see the von Mises equivalent stresses σ_{v} in the lower endplate of the fourth and the upper endplate of the fifth vertebral body, respectively, which are of special interest for a biomechanical engineer examining bone remodeling processes. On the right hand side we have depicted the respective cuts through the fourth and the fifth vertebral body with σ_{v}. For more details we refer to [13] and the bibliography therein.

As already mentioned, our mortar discretization can also be used to simulate the transmission of forces for multi-body contact problems with Coulomb friction. Here, we do not go into detail but, instead, give one short example and refer to [32] for the development of a non-smooth multigrid solver for frictional multi-body contact. We consider the geometry with the wavy potential contact boundary from problem (d), choose the same material parameters as before, and set the coefficient of friction to 0.2. Similar to the earlier problem settings, we prescribe Dirichlet boundary values $(0, 0, \mp 0.025)$ for the displacements at the upper/lower face of the upper/lower body, respectively, and homogeneous Neumann boundary conditions elsewhere. Then, Figure 15 shows the component $\boldsymbol{\sigma}_t \cdot \boldsymbol{e}_1$ of the resulting tangential stresses, which just like the normal stresses are perfectly resolved despite their non-smooth shape.

6.4. Direct solver versus multigrid method. Finally, we exemplarily compare the performances of the monotone multigrid method [30, 31] and the sparse direct

l	# dof	direct solver (linear)	peak memory for decomposition	multigrid method (linear)	multigrid method (contact)
2	750	0.2 s	0.8 MB	0.3 s	0.5 s
3	4,374	2.3 s	12.5 MB	2.6 s	4.0 s
4	29,478	45.8 s	190.4 MB	23.4 s	33.3 s
4^*	122,550	781.1 s	1,667.2 MB	97.9 s	155.4 s
5	215,622	2,737.1 s	3,124.4 MB	199.6 s	259.3 s
5^*	931,686	—	—	865.8 s	1,650.3 s
6	1,647,750	—	—	1,668.6 s	3,329.0 s

FIG. 16. *Sparse direct solver versus monotone multigrid method: time needed to solve problem (a).*

solver [43]. For this purpose, we measure the time needed to solve problem (a) for different numbers of degrees of freedom, see Figure 16. Of course the direct solver can only be applied to the linear problem arising if the contact constraints are ignored. For the multigrid solver we choose a $\mathcal{W}(1,1)$-cycle and write down the time needed to solve the linear unconstrained problem as well as to solve the nonlinear contact problem. Note that, as before, we use $||\tilde{\boldsymbol{u}}_{h_l} - \boldsymbol{u}_{h_l}||_{\boldsymbol{X}} \leq 10^{-10}$ as stopping criterion, which is very strict in case of engineering applications. In addition to the familiar levels $l = 2, \ldots, 6$ the meshes for $l = 4^*$ and $l = 5^*$ are generated from the respective meshes on level $l = 4$ and $l = 5$ by refining the upper body only.

The data in Figure 16 clearly show the superiority of the multigrid method. Due to the large amount of main memory the sparse solver has to allocate to compute the decomposition, the largest directly solvable problem on the employed machine was for $l = 5$. However, on the same machine, with the monotone multigrid method a *nonlinear* problem almost eight times larger can be solved in about 6/5 of the time the sparse solver needs for the smaller *linear* problem.

Acknowlegdements. The authors would like to thank Sebastian Paik for the implementation of the modified simplex algorithm and help with the integration of the octree component, the group of Hanns Ruder at University of Tübingen and Color-Physics GmbH for the inspiring collaboration in biomechanics, and the Deutsche Forschungsgemeinschaft (SFB 611, Hausdorff Center for Mathematics, and Bonn International Graduate School in Mathematics) for various financial support.

REFERENCES

[1] Ainsworth H. Octree C++ general component. 2005.
[2] Barber C M, Dobkin D P, Huhdanpaa H. The quickhull algorithm for convex hulls. *ACM Transactions on Mathematical Software* 1996; **22**(4):469–483.
[3] Bastian P, Birken K, Johannsen K, Lang S, Neuß N, Rentz-Reichert H, Wieners C. UG – a flexible software toolbox for solving partial differential equations. *Computing and Visualization in Science* 1997; **1**:27–40.
[4] Ben Belgacem F. The mortar finite element method with Lagrange multipliers. *Numerische Mathematik* 1999; **84**:173–197.
[5] Ben Belgacem F, Hild P, Laborde P. Extension of the mortar finite element method to a variational inequality modeling unilateral contact. *Mathematical Models & Methods in Applied Sciences* 1999; **9**(2):287–303.
[6] Ben Belgacem F, Maday Y. The mortar finite element method for three dimensional finite elements. *Modélisation Mathématique et Analyse Numérique* 1997; **31**(2)289–302.
[7] Bernardi C, Maday Y, Patera A T. A new nonconforming approach to domain decomposition: the mortar element method. In *Nonlinear partial differential equations and their appli-*

cations, Brezis H, Lions J L (eds). Pitman Research Notes in Mathematics 299. Harlow: Longman Scientific & Technical: New York, 1994; 13–51.

[8] Bernardi C, Maday Y, Rapetti F. Basics and some applications of the mortar element method. *GAMM-Mitteilungen* 2005; **28**(2):97–123.

[9] Boieri P, Gastaldi F, Kinderlehrer D. Existence, uniqueness, and regularity results for the two-body contact problem. *Applied Mathematics and Optimization* 1987; **15**:251–277.

[10] Braess D, Dahmen W. Stability estimates of the mortar finite element method for 3-dimensional problems. *East-West Journal of Numerical Mathematics* 1998; **6**(4):249–264.

[11] Ciarlet P G. *Mathematical Elasticity, Vol. I: Three-Dimensional Elasticity.* Studies in Mathematics and its Applications 20. North-Holland: Amsterdam, 1988.

[12] Coorevits P, Hild P, Lhalouani K, Sassi T. Mixed finite element methods for unilateral problems: convergence analysis and numerical studies. *Mathematics of Computation* 2002; **71**(237):1–25.

[13] Dickopf T. Konstruktion stabiler Kopplungsoperatoren für Mehrkörperkontaktprobleme und Anwendungen in der Biomechanik. Diplomarbeit, Universität Bonn, 2007.

[14] Eck C. Existenz und Regularität der Lösungen für Kontaktprobleme mit Reibung. PhD thesis, Universität Stuttgart, 1996.

[15] Eck C, Wohlmuth B. Convergence of a contact-Neumann iteration for the solution of two-body contact problems. *Mathematical Models & Methods in Applied Sciences* 2003; **13**(8):1103–1118.

[16] Falletta S. The approximate integration in the mortar method constraint. In *Domain Decomposition Methods in Science and Engineering XVI,* Widlund O B, Keyes D E (eds). Lecture Notes in Computational Science and Engineering 55. Springer: Berlin, 2007; 555–563.

[17] Flemisch B, Melenk J M, Wohlmuth B. Mortar methods with curved interfaces. *Applied Numerical Mathematics* 2005; **54**(3–4):339–361.

[18] Flemisch B, Puso M A, Wohlmuth B. A new dual mortar method for curved interfaces: linear elasticity. *International Journal for Numerical Methods in Engineering* 2005; **63**(6):813–832.

[19] Flemisch B, Wohlmuth B. Stable Lagrange multipliers for quadrilateral meshes of curved interfaces in 3d. *Computer Methods in Applied Mechanics and Engineering* 2007; **196**(8):1589–1602.

[20] Groß C. Import of geometries and extended informations into Obslib++ using the Exodus II and Exodus parameter file formats. INS Preprint No. 0712, Universität Bonn, 2007.

[21] Haslinger J, Hlaváček I, Nečas J. Numerical methods for unilateral problems in solid mechanics. In *Handbook of Numerical Analysis,* Ciarlet P G, Lions J L (eds). North-Holland: Amsterdam, 1996; 313–485.

[22] Hauret P, Le Tallec P. A stabilized discontinuous mortar formulation for elastostatics and elastodynamics problems. Part II: discontinuous Lagrange multipliers. Technical Report 554, Ecole Polytechnique, Centre de Mathématiques Appliquées, 2004.

[23] Hild P. A propros d'approximation par éléments finis optimale pour les problèmes de contact unilatéral. *Comptes Rendus de l'Académie des Sciences. Série I. Mathématique* 1998; **326**(10):1233–1236.

[24] Hild P. Numerical implementation of two nonconforming finite element methods for unilateral contact. *Computer Methods in Applied Mechanics and Engineering* 2000; **184**:99–123.

[25] Hüeber S, Stadler G, Wohlmuth B. A primal-dual active set algorithm for three-dimensional contact problems with Coulomb friction. *SIAM Journal on Scientific Computing* 2008; **30**(2):572–596.

[26] Hüeber S, Wohlmuth B. An optimal a priori error estimate for non-linear multibody contact problems. *SIAM Journal on Numerical Analysis* 2005; **43**(1):157–173.

[27] Hüeber S, Wohlmuth B. A primal-dual active set strategy for non-linear multibody contact problems. *Computer Methods in Applied Mechanics and Engineering* 2005; **194**(27–29):3147–3166.

[28] Kikuchi N, Oden J T. *Contact Problems in Elasticity: A Study of Variational Inequalities and Finite Element Methods.* Studies in Applied Mathematics 8. SIAM: Philadelphia, 1988.

[29] Kim C, Lazarov R D, Pasciak J E, Vassilevski P S. Multiplier spaces for the mortar finite element method in three dimensions. *SIAM Journal on Numerical Analysis* 2001; **39**(2):519–538.

[30] Kornhuber R, Krause R. Adaptive multigrid methods for Signorini's problem in linear elasticity. *Computing and Visualization in Science* 2001; **4**(1):9–20.

[31] Krause R. Monotone Multigrid Methods for Signorini's Problem with Friction. PhD thesis, Freie Universität Berlin, 2001.

[32] Krause R. A non-smooth multigrid method for solving frictional two-body contact problems in 2d and 3d with multigrid efficiency. INS Preprint No. 0602, Universität Bonn, 2006.

[33] Krause R, Sander O. Fast solving of contact problems on complicated geometries. In *Domain Decomposition Methods in Science and Engineering,* Kornhuber R et al (eds). Lecture Notes in Computational Science and Engineering 40. Springer: Berlin, 2005; 495–502.
[34] Krause R, Wohlmuth B. Nonconforming domain decomposition techniques for linear elasticity. *East-West Journal of Numerical Mathematics* 2000; **8**(3):177–206.
[35] Lamichhane B. Higher order mortar finite elements with dual Lagrange multiplier spaces and applications. PhD thesis, Universität Stuttgart, 2006.
[36] Laursen T A. *Computational Contact and Impact Mechanics.* Springer: Berlin, 2002.
[37] Le Tallec P, Sassi T. Domain decomposition with nonmatching grids: augmented Lagrangian approach. *Mathematics of Computation* 1995; **64**(212):1367–1396.
[38] Lhalouani K, Sassi T. The mortar finite element method for some problems of unilateral contact with non-local Coulomb's friction. Technical Report UMR 5585, Laboratoire de Mécanique des Contacts, Institue National des Sciences Appliquées de Lyon, 1999.
[39] Lions J L, Stampacchia G. *Variational inequalities.* Communications on Pure and Applied Mathematics 1967; **20**(3):493–519.
[40] Maday Y, Rapetti F, Wohlmuth B. The influence of quadrature formulas in 2d and 3d mortar element methods. In *Recent Developments in Domain Decomposition Methods,* Pavarino L F, Toselli A (eds). Lecture Notes in Computational Science and Engineering 23. Springer: Berlin, 2002; 203–221.
[41] Puso M A. A 3D mortar method for solid mechanics. *International Journal for Numerical Methods in Engineering* 2004; **59**:315–336.
[42] Puso M A, Laursen T A. A mortar segment-to-segment contact method for large deformation solid mechanics. *Computer Methods in Applied Mechanics and Engineering* 2004; **193**(6–8):601–629.
[43] Schenk O, Gärtner K. Solving unsymmetric sparse systems of linear equations with PARDISO. *Journal of Future Generation Computer Systems* 2004; **20**(3)475–487.
[44] Wohlmuth B. *Discretization Methods and Iterative Solvers Based on Domain Decomposition.* Lecture Notes in Computational Science and Engineering 17. Springer: Berlin, 2001.
[45] Wohlmuth B, Krause R. Monotone multigrid methods on nonmatching grids for nonlinear multibody contact problems. *SIAM Journal on Scientific Computing* 2003; **25**(1)324–347.
[46] Wriggers P. *Computational Contact Mechanics.* John Wiley & Sons: Chichester, 2002.

Bestellungen nimmt entgegen:

Institut für Angewandte Mathematik
der Universität Bonn
Sonderforschungsbereich 611
Wegelerstr. 6
D - 53115 Bonn

Telefon: 0228/73 4882
Telefax: 0228/73 7864
E-mail: astrid.link@iam.uni-bonn.de http://www.sfb611.iam.uni-bonn.de/

Verzeichnis der erschienenen Preprints ab No. 370

370. Han, Jingfeng; Berkels, Benjamin; Droske, Marc; Hornegger, Joachim; Rumpf, Martin; Schaller, Carlo; Scorzin, Jasmin; Urbach Horst: Mumford–Shah Model for One-to-one Edge Matching; erscheint in: IEEE Transactions on Image Processing

371. Conti, Sergio; Held, Harald; Pach, Martin; Rumpf, Martin; Schultz, Rüdiger: Shape Optimization under Uncertainty – a Stochastic Programming Perspective

372. Liehr, Florian; Preusser, Tobias; Rumpf, Martin; Sauter, Stefan; Schwen, Lars Ole: Composite Finite Elements for 3D Image Based Computing

373. Bonciocat, Anca-Iuliana; Sturm, Karl-Theodor: Mass Transportation and Rough Curvature Bounds for Discrete Spaces

374. Steiner, Jutta: Compactness for the Asymmetric Bloch Wall

375. Bensoussan, Alain; Frehse, Jens: On Diagonal Elliptic and Parabolic Systems with Super-Quadratic Hamiltonians

376. Frehse, Jens; Specovius-Neugebauer, Maria: Morrey Estimates and Hölder Continuity for Solutions to Parabolic Equations with Entropy Inequalities

377. Albeverio, Sergio; Ayupov, Shavkat A.; Omirov, Bakhrom A.; Turdibaev, Rustam M.: Cartan Subalgebras of Leibniz n-Algebras

378. Schweitzer, Marc Alexander: A Particle-Partition of Unity Method – Part VIII: Hierarchical Enrichment

379. Schweitzer, Marc Alexander: An Algebraic Treatment of Essential Boundary Conditions in the Particle–Partition of Unity Method

380. Schweitzer, Marc Alexander: Stable Enrichment and Local Preconditioning in the Particle–Partition of Unity Method

381. Albeverio, Sergio; Ayupov, Shavkat A.; Abdullaev, Rustam Z.: Arens Spaces Associated with von Neumann Algebras and Normal States

382. Ohta, Shin-ichi: Finsler Interpolation Inequalities

383. Fang, Shizan; Shao, Jinghai; Sturm, Karl-Theodor: Wasserstein Space Over the Wiener Space

384. Nepomnyaschikh, Sergey V.; Scherer, Karl: Multilevel Preconditioners for Bilinear Finite Element Approximations of Diffusion Problems

385. Albeverio, Sergio; Hryniv, Rostyslav; Mykytyuk, Yaroslav: Factorisation of Non-Negative Fredholm Operators and Inverse Spectral Problems for Bessel Operators

386. Otto, Felix: Optimal Bounds on the Kuramoto-Sivashinsky Equation

387. Gottschalk, Hanno; Thaler, Horst: A Comment on the Infra-Red Problem in the AdS/CFT Correspondence

388. Dickopf, Thomas; Krause, Rolf: Efficient Simulation of Multi-Body Contact Problems on Complex Geometries: A Flexible Decomposition Approach Using Constrained Minimization